Received 00th January 20xx,
Accepted 00th January 20xx

DOI: 10.1039/x0xx00000x

www.rsc.org/

An Experimental and Theoretical Study of the Magnetic Relaxation in Heterometallic Coordination Polymers Based on 6-methyl-2-oxonicotinate and Lanthanide(III) Ions with Square Antriprismatic Environment

Laura Razquin-Bobillo,[a] Oier Pajuelo-Corral,[a] Andoni Zabala-Lekuona,[a] Antonio Rodríguez-Diéguez[b] and Javier Cepeda*[,a]

Two new isostructural compounds based on 6-methyl-2-oxonicotinate (6m2onic) ligand and sodium and lanthanide(III) ions are reported. The structural and chemical characterization reveals the following chemical formula: {[Ln(6m2onic)$_2$(μ-6m2onic)$_2$Na(H$_2$O)$_3$]·8H$_2$O}$_n$ [where Ln(III) = Dy (**1**$_{Dy}$) and Er (**2**$_{Er}$)]. These compounds crystallize in the form of one-dimensional arrays held together into a hydrogen-bonded structure, in which 6m2onic ligands establish four O,O' chelating rings with the lanthanide to render a distorted square antiprism (SAPR) geometry. Magnetic *dc* and *ac* susceptibility measurements confirm that **1**$_{Dy}$ and **2**$_{Er}$ behave as SIMs. Magnetic dilutions using Y(III) matrices have been made to achieve a Dy(III) counterpart (**1**$_{Y/Dy}$) that presents slow magnetic relaxation under zero *dc* field. Under an optimized H_{dc} field (of 1000 Oe and 1500 Oe for **1**$_{Y/Dy}$ and **2**$_{Y/Er}$, respectively), **1**$_{Y/Dy}$ reveals the occurrence of two well-separated maxima, attributed to SR (U_{eff} = 65.2 K (45.3 cm^{-1}) and $\tau_0 = 2.76\cdot10^{-9}$ s) and FR processes (U_{eff} = 23.2 K (16.1 cm^{-1}) and $\tau_0 = 1.40\cdot10^{-8}$ s), whereas **2**$_{Y/Er}$ shows a multiple relaxation pathway that considers quantum tuneling of the magnetization (QTM), Orbach, Raman and Direct mechanisms. *Ab initio* calculations have been carried out to support the experimental evidence and to explain the lanthanide ion-dependent behaviour deepen the understanding of the magneto-structural relationship of the SAPR environment.

Introduction

The possibility of combining, in a crystalline material, various physical properties and thrilling structures has turned coordination polymers (CPs), and the particular subclass of metal-organic frameworks (MOFs), into very attractive compounds for scientists working in the field of coordination chemistry owing to their wide variety of applications.[1–4] A key point of this success derives from the possibility of combining the appropriate starting components (metal ions and ligands), in such a way that they render the desired metal-organic architecture when they are self-assembled during the crystallization,[5–7] somehow controlling the final properties of the compound.[8,9] In addition to the porous features of these materials, which give rise to tuneable and ultraporous frameworks with high gas capture capacity and separation,[10–12] other equally fascinating properties arise from non-porous CPs, such as photoluminescence, conductivity or molecular magnetism.[13–19] In this regard, magnetic CPs have awakened high interest for designing materials with sensing, magnetic sequestration and stimuli-responsive abilities.[17,20,21] Owing to the low capacity of most of organic ligands to transmit significant long-range exchange interactions, single-ion magnets (SIMs) are preferred for this purpose because their magnetic response is intrinsic to the metal centre.[22–26] This new subclass of molecular magnets, in which the slow relaxation of the magnetization (SRM) is derived from mononuclear lanthanide ions, have demonstrated the same potential applications attributed to SMMs, i.e. high-density data storage, quantum computing, molecular spintronics and enhancing the pseudocontact shift in nuclear magnetic resonance.[27–29]

To date, the spin dynamics of SIMs are not fully understood due to the major role played by molecular vibrations,[21] despite of which recent theoretical efforts have provided guidance on the synthesis of new SIMs to allow reaching record values of T_B = 80 K.[30,31] In this sense, some studies have found that the interplay between local anisotropy of lanthanide ions, crystal field effects, coordination geometry and dipolar spin–spin interactions is critical for optimizing the performance of SIMs.[32,33] In particular, one major idea to achieve high-performance SIMs focuses on the charge distribution around the lanthanide ion, since high-order symmetries such as C_∞, D_{5h} and D_{4d} are beneficial for the suppression of quantum tunnelling of the magnetization (QTM) when the magnetic anisotropy is appropriate.[34,35] Among these polyhedra, most of

[a] Departamento de Química Aplicada, Facultad de Química, Universidad del País Vasco/Euskal Herriko Unibertsitatea (UPV/EHU), 20018 Donostia-San Sebastián, Spain. E-mail: javier.cepeda@ehu.es
[b] Departamento de Química Inorgánica, UEQ, C/ Severo Ochoa s/n, Universidad de Granada, 18071, Granada, Spain.

† Footnotes relating to the title and/or authors should appear here.
Electronic Supplementary Information (ESI) available: [details of any supplementary information available should be included here]. See DOI: 10.1039/x0xx00000x

the reported lanthanide(III)-based SIMs exhibit square antiprismatic (SAPR) environment. In this polyhedron, it is well known that small changes in the donor set, ligand field strength and the low predictable inter-molecular interactions could regulate the anisotropy and tune the magnetic dynamics of the compound. In fact, some important exceptions have been found to the concept by Rinehart and Long[26] by which the optimal crystal field environment that enhances the SMM behaviour is that which better adapts to the prolate/oblate shaped electron cloud of the lanthanide ion. For instance, it predicts that sandwich-like environments with ligand electron density placed above and below the *xy* plane, such as well known Cp ligands,[36–39] maximizes the anisotropy of oblate ions such as Dy(III), which is the most extensively employed ion because of its large magnetic moment and significant anisotropy derived from unquenched orbital angular momentum.[40] However, as proven by Murugesu and coworkers,[41] the SIM behaviour is enhanced in an Er(III)-COT analogue even if that ion presents prolate shaped nature and COT, a ligand which might be initially categorized in the same group of Cp-based complexes. Therefore, it is of vital necessity to get a deeper insight into the structure–magnet performance relationship of SAPR Ln-SIMs in order to design SIMs with enhanced U_{eff} and T_B.

To that end, and continuing with our relentless quest for multifunctional materials behaving as SIMs,[24,42–44] in the present work we have resorted to the potential of the 6-methyl-2-oxonicotinate ligand (6m2onic) to build SAPR-like environments owing to its carboxylate/ketone moiety that establishes chelating rings resembling those of previously reported β-diketonato ligands.[45–48] Moreover, with this arrangement the occurrence of additional links enabling superexchange bridges with neighbouring paramagnetic ions would be prevented. Two isostructural compounds based on different lanthanide(III) ions with both oblate and prolate electron clouds have been employed to explore the effects of the LnO_8 coordination environment on the SRM, for which a detailed study of the magnetic properties combined with *ab initio* calculations has been accomplished.

Results and Discussion

Comments on the synthesis of Ln/Na/H2h6mnic system

In the present work, the reported ternary compounds are achieved from a mixture containing the corresponding lanthanide(III) nitrate, sodium hydroxide and the acid form of the ligand (H2h6mnic). It is worth noticing the fact that the latter undergoes a prototropy that involves the migration of the hydroxyl hydrogen atom to the pyridinic nitrogen, which results in an N–H group that yields the 6-methyl-2-oxonicotinate ligand (6m2onic). This equilibrium has been previously observed for other previously published compounds based on this ligand,[49,50] and it seems to be pushed by the formation of a six-membered chelating ring with the metal ion formed by the ketone and adjacent carboxylate oxygen atoms, a structural feature that defines the coordination environment of the present compounds. In this sense, it has been observed that the free ligand itself undergoes the prototropic reaction in water solution since H6m2onic is the final crystallization product when H2h6mnic is dissolved.[49] This result must be attributed to the hydrogen bonding interactions occurring in the crystal structure of H6m2onic because, as confirmed in our previous work in which both ligands have been optimized at DFT level, H2h6mnic tautomer is indeed the most stable molecule.[50] On the other hand, it is also worth mentioning that the compound requires the addition of sodium hydroxide not only for the presence of sodium cation in the medium but also for meeting a more basic solution that favours the deprotonation of the ligand (see Scheme 1).

Structural description of $\{[Ln(6m2onic)_2(\mu\text{-}6m2onic)_2Na(H_2O)_3]\cdot 8H_2O\}_n$ [where Ln(III) = Dy ($\mathbf{1_{Dy}}$) and Er ($\mathbf{2_{Er}}$)]

The synthesised CPs are isostructural, as revealed the analysis of the X-ray diffraction data, and crystallize in the *Pbca* space group in the form of one-dimensional arrays. Therefore, compound $\mathbf{1_{Dy}}$ will be described as a representative counterpart. The asymmetric unit consists of a dysprosium(III) metal atom, Dy1, a sodium(I) atom, Na2, four 6m2onic ligands and eleven water molecules (distinguishing between three coordinated and eight lattice molecules). The Dy1 atom is coordinated by eight oxygen atoms (four ketone and four carboxylate oxygens) from the four chelating 6m2onic ligands (labelled A, B, C and D), rendering an environment that resembles a square antiprism as confirmed by continuous shape measures (CShMs, S_{SAPR} = 0.458), although it is not too far from other classical geometries such as biaugmented trigonal prism (BTPR) and triangular dodecahedron (TDD, see ESI). The second centre (that surrounding Na2 atom) is established by a NaO_6 chromophore that renders a distorted octahedron according to CShMs (Figure 1). Such a coordination polyhedron is less frequent among sodium ions in coordination chemistry, which habitually acquire higher coordination indices, although some examples with coordination number equal to five have been also reported.[51–53] Two of the donor oxygen atoms pertain to two 6m2onic molecules, one of which belongs to a carboxylate group (of the C ligand) and the other to the ketone group (of a copy of D ligand). It is worth considering that the second carboxylate oxygen atom (O31C) could be somehow interacting with Na1 atom, a fact that would bring the sixth donor atom to the coordination sphere. The remaining three oxygen atoms belong to coordination water molecules. Table 1 gathers the coordination bond Dy-O and Na-O distances, which fall within the usual range bounded by other reported compounds.

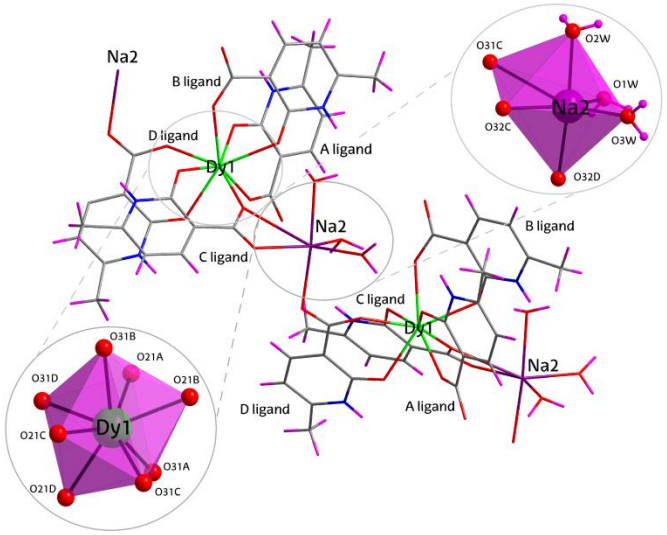

Figure 1. Polymeric structure and coordination polyhedra of compound $\mathbf{1_{Dy}}$. Colour coding: carbon (grey), nitrogen (blue), oxygen (red), hydrogen (pink), dysprosium (green) and sodium (purple).

Table 1. Selected bond lengths for compound $\mathbf{1_{Dy}}$ (Å).[a]

Coordination sphere of the Dy1 atom			
Dy1–O21A	2.391(1)	Dy1–O21C	2.334(1)
Dy1–O31A	2.332(1)	Dy1-O31C	2.321(1)
Dy1–O21B	2.405(1)	Dy1-O21D	2.372(1)
Dy1–O31B	2.395(1)	Dy1–O31D	2.309(1)
Coordination sphere of the Na2 atom			
Na2–O31C	2.940(1)	Na2–O1W	2.379(1)
Na2–O32C	2.322(1)	Na2–O2CW	2.444(1)
Na2–O32D(i)	2.373(1)	Na2–O3W	2.305(1)

[a] *Symmetries: (i) x-1/2, y, -z+1/2.*

The relative arrangement of the four independent ligands around the Dy1 atom is worth to be highlighted, because they are organized in pairs (A and B ligands on the one hand, and C and D on the other) such that their aromatic rings are displaced almost parallel as to maximize the interactions between their π clouds. The coordination water molecules also favour the previous arrangement by establishing strong intramolecular hydrogen bonds with neighbouring 6m2onic ligands. Concerning their linkage, the ligands show three coordination modes depending on their binding to the two metal ions. First, ligands A and B are bonded to the central Dy1 atom via six-membered chelate rings with the κ^2O21,O31 mode. On its part, ligand C also employs, in addition to the previous ring, both carboxylate oxygen atoms to form a four-membered chelating ring, thus showing the μ-κ^2*O21*,*O31*:κ^2*O31*,*O32* mode. Finally, ligand D acquires the μ-κ^2*O21*,*O31*:κ*O32* mode that imposes the latter connectivity on the compound although it does not form the second chelating ring. Note that these last two ligands act as a bridge between consecutive Dy1 and Na2 along the coordination chains running parallel to the [100] crystallographic direction, imposing distances of ca. 4.96 and 5.20 Å, respectively for C and D ligands (see ESI). The metal-organic chains are joined one another by means of hydrogen bonding interactions mediated by the crystallisation water molecules, since all the heteroatoms potentially establishing hydrogen bonds get towards the chain. As a result, the lanthanide ions are isolated from each other by the insertion of the sodium atom into the chain, so that the minimum Dy···Dy distance is 9.461 Å between neighbouring chains (Figure 2).

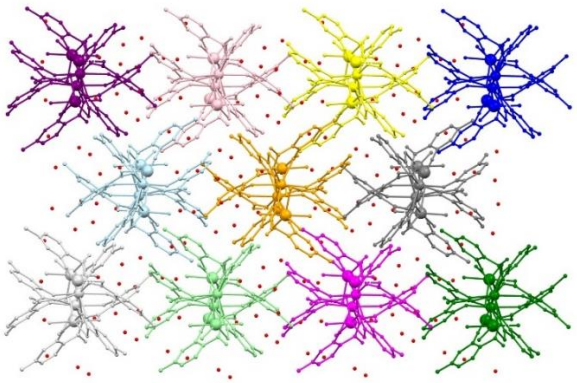

Figure 2. Crystal packing of compound $\mathbf{1_{Dy}}$ showing the metal-organic chains (in different colours) in the propagation direction (along crystallographic *a* axis). Crystallization water molecules are shown in red colour.

Magnetic measurements

Static magnetic properties

The static magnetic properties were determined by measuring the *dc* magnetic susceptibilities of polycrystalline samples of the compounds in the temperature range of 2–300 K under an applied field of 0.1 T. As observed in Figure 3, the room temperature values of the $\chi_M T$ product are close to those calculated for an isolated Ln(III) ion using the free-ion approximation (Table 2). Upon cooling, the $\chi_M T$ product steadily decreases up to 50 K, and more pronounced at low temperature owing to the depopulation of the excited m_J sublevels arising from the splitting of the ground spin-orbit terms of the Ln(III) ions by the ligand field. Despite the fact that antiferromagnetic exchange interactions among the paramagnetic ions could also be behind this behaviour, the large Ln···Ln distances (above 9.4 Å) found in the crystal structure make this possibility less likely to be significant. The field-dependence of the magnetization measured at various temperatures is characteristic of a single isolated Ln(III) centre, exhibiting a relatively rapid increase in the magnetization at low field to reach almost saturation at an H_{dc} of 7 T. The observed saturation values are lower than those calculated for the free-ion, a fact that is due to crystal-field effects leading to sizeable magnetic anisotropy in the compounds.[54,55] The latter effect is also inferred from the reduced magnetization plots (see Figure S5 in the ESI), where the curves for different applied fields are not superimposed to each other, especially for the case of $\mathbf{1_{Dy}}$.

Table 2. *Dc* magnetic data for the compounds.

Ground state of Ln(III) ion	Theor. $\chi_M T$ value ($cm^3\ mol^{-1}\ K$)	Exp. $\chi_M T$(300K)/ $\chi_M T$(2K) values ($cm^3\ mol^{-1}\ K$)
Dy(III), $^6H_{15/2}$, g_J = 4/3	14.17	14.25 / 9.95
Er(III), $^4I_{5/2}$, g_J = 6/5	11.48	11.52 / 7.38

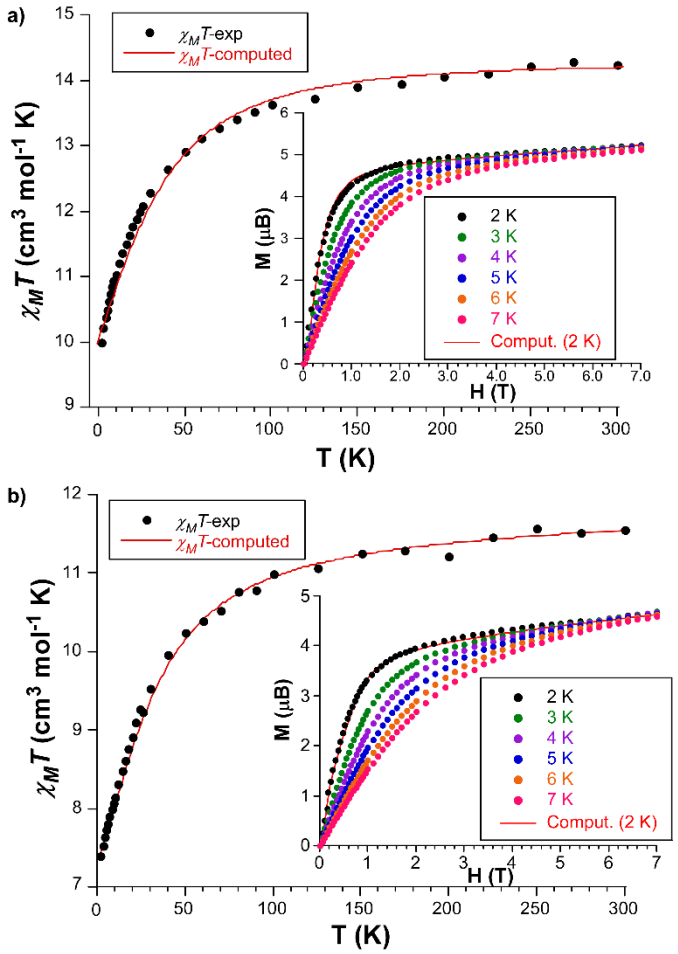

Figure 3. Thermal dependence of $\chi_M T$ for compounds $\mathbf{1}_{Dy}$ and $\mathbf{2}_{Er}$ with the computed result. Insets show the isothermal magnetization curves measured at variable temperature with the computed curve at 2 K for both compounds.

Dynamic magnetic properties

Alternating current (*ac*) magnetic susceptibility measurements were conducted on polycrystalline samples of all compounds in order to study their SMM behaviour arising from the single-ion magnetic anisotropy. To start with, the curves were recorded under an *ac* field of 3.5 Oe and zero *dc* field, finding that $\mathbf{1}_{Dy}$ is the only one that shows temperature-dependent signals in the out-of phase (χ_M'') curves (see Figures S7-8). In particular, the curve recorded at 10000 Hz in the χ_M''(T) plot presents a maximum around 7 K followed by a steep rise down to 2 K, which is a characteristic of QTM. The magnetic response is strongly boosted under an applied *dc* field of 1000 Oe, since the χ_M'' curve clearly shows the presence of two maxima peaking at 2.8 and 7.2 K, which corroborates a single-ion magnet behaviour in the compound as expected for the axial ground KD in $\mathbf{1}_{Dy}$ (vide infra in *ab initio* calculations). The fact of observing two maxima may be attributed to the occurrence of two magnetic relaxation processes corresponding to fast (FR) and a slow (SR) relaxation phase, as previously denoted for other compounds.[56,57] The existence of two thermally activated processes is completely unexpected in this case owing to the crystallization of a unique Dy1 atom in the structure. However, such behaviour is not unprecedented but it has been previously reported for both Ln(III)- and Co(II)-based compounds, where multiple origins have been alluded including the presence of two conformers in the framework, the interplay between molecular/dipolar interactions or even a phenomenon inherent to Co(II) ion have been argued to justify the behaviour.[58–61]

In order to know if this two-step relaxation stems from an intra- or intermolecular origin, a magnetic dilution of the compound was performed by crystallizing the Dy(III) ions into the diamagnetic Y(III)-based analogue (10% of Dy(III), compound $\mathbf{1}_{Y/Dy}$ hereafter). As observed in Figure 4a, the χ_M'' curves collected at several frequencies are much better defined than in the pure Dy-based compound $\mathbf{1}_{Dy}$ due to the absence of Ln···Ln interactions in the diluted compound $\mathbf{1}_{Y/Dy}$. At zero applied *dc* field, the Cole-Cole plots were fitted in the 5.2-7.6 K temperature range due to the fact that the data of low temperature is affected by the hidden maxima (Figure S10a). This is also noticeable in the $\chi_M''(\upsilon)$ curves (Figure S11a). In this case, the curves at 5.2-5.6 K are influenced by a second maximum occurring at the highest frequencies, but not clearly detected in the χ_M''(T) curves. The presence of this second maximum is not unexpected considering that when measuring at $H_{dc} \neq 0$ two well defined sets of maxima are found related to FR and SR. The relatively large α values obtained, ranging between 0.37 and 0.20, are usually attributed to the presence of several simultaneous relaxation mechanisms. In this case, however, we should consider the second relaxation process occurring at the lowest temperatures, which must be the reason of those large α values at the lowest fitted temperatures. A glance to the frequency (Freq)-dependent χ_M'' signals shows that the maxima, representative for the high-temperature process, are shifted to higher frequencies as the temperature rises. Fitting of these data to the generalized Debye model affords the relaxation times of the magnetization (τ) at each temperature. The distribution of these τ fit reasonably well to a linear distribution, meaning that Orbach process might be the main responsible for the magnetic relaxation of the compound. The effective energy barrier for the reversal of the magnetization (U_{eff}) and the pre-exponential factor τ_0 extracted from the fit of τ in the high temperature region (5.3–7.6 K) to the Arrhenius law (see equation 1) are 43.5 K (30.3 cm^{-1}) and 4.41 10^{-8} s (see inset in Figure 4a and Table 3).

$$\tau^{-1} = \tau_0^{-1} \exp(-U_{eff}/\kappa_B T) \qquad \text{(eq. 1)}$$

Table 3. Best fitting results from experimental magnetic *ac* measurements.

Comp.	*dc* field (Oe)	Fitting T (K)	U_{eff} (K/cm^{-1})	τ_0 (s)	τ_{QTM} (s)	A_{direct} (s^{-1} K^{-1})	B_{Raman}/n (s^{-1} K^{-n})
$\mathbf{1}_{Y/Dy}$	H_{dc} = 0	5.3–7.6	43.5/30.3	4.41 10^{-8}			
	H_{dc} = 1000	2.8–3.2	23.2/16.1	1.40·10^{-8}			
		5.0–7.6	65.2/45.3	2.76·10^{-9}			
$\mathbf{2}_{Y/Er}$	H_{dc} = 1500	2.0–3.6	7.0/4.9	1.75·10^{-5}			
		3.8–4.8	28.3/19.7	5.58·10^{-8}			
		2.0–4.8	58.5/40.7	1.47·10^{-10}	247	88.9	187/2.9

With the double aim of further characterizing the slow relaxation phenomenon and studying the effect of the *dc* field, the latter was scanned by recording the magnetic susceptibility at 5 K. As it can be seen in Figure S12 in the ESI, the relaxation

is substantially prolonged above 500 Oe to present the optimal relaxation at 1000 Oe range, so the measurements were repeated under an H_{dc} = 1000 Oe. The application of such external field on compound **1**$_{Y/Dy}$ brings a slight but effective increase of the signal intensity for the high temperature maxima and, importantly, it shifts the low temperature maxima above 2K allowing to visualize those corresponding to most of frequencies. Unlike to what happened under zero field, we were able to estimate the τ values for each separated regime (Figure S11b).[62] The Arrhenius plots constructed for both processes give the following two sets of parameters: U_{eff} = 23.2 K (16.1 cm^{-1}) and $\tau_0 = 1.40 \cdot 10^{-8}$ s for the low- and U_{eff} = 65.2 K (45.3 cm^{-1}) and $\tau_0 = 2.76 \cdot 10^{-9}$ s for the high-temperature processes, which have been named as FR and SR, respectively.

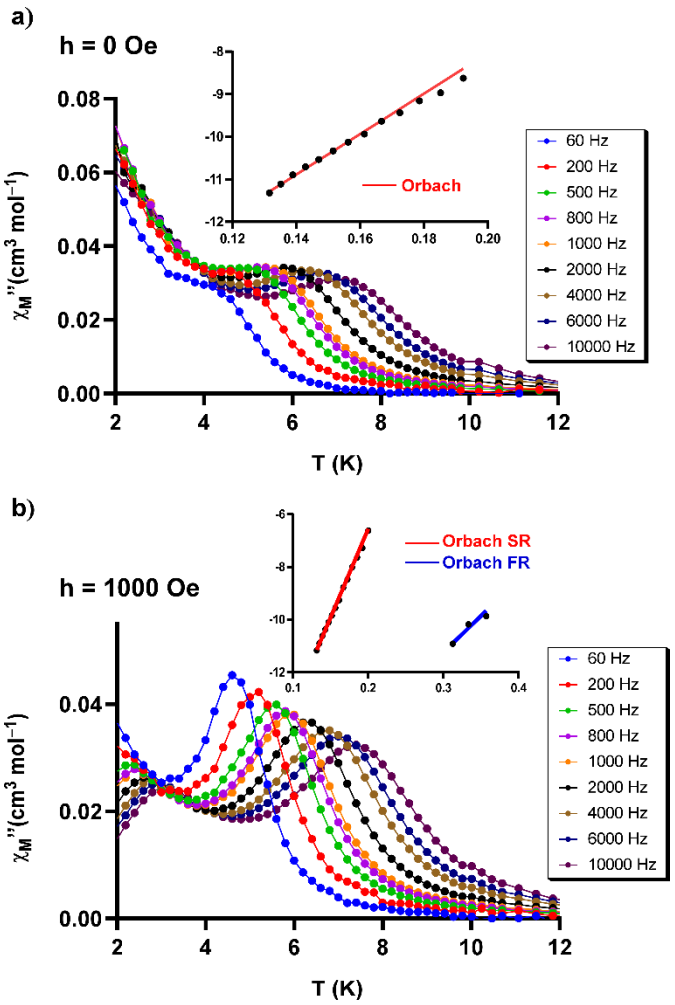

Figure 4. Temperature dependence of the χ_M'' signals for the diluted compound **1**$_{Y/Dy}$ under **(a)** zero *dc* field and **(b)** an applied *dc* field of 1000 Oe. Inset shows the temperature dependence for the relaxation times and best Arrhenius fits of the data.

In the case of the Er-based compound, the diluted sample of compound **2**$_{Y/Er}$ neither shows Freq dependent maxima in the absence of *dc* field whereas the application of an arbitrary field of H_{dc}=1000 Oe promotes the onset of a signal in the χ_M'' vs T plot for the highest Freq (10000 Hz, see Figure S13). The signal is characterized by a main maximum centred at 4–5 K range accompanied by a wide and weak contribution at low temperature. In view of this event, additional measurements were conducted to optimize the external *dc* field that improves the SMM behaviour of the compound, for which isothermal curves (at 2.8 K) were measured under variable field and oscillating Freq. As observed in Figure S17 (see ESI), the relaxation time exhibits an inverted U-shaped distribution in the τ vs H plot with the maximum around 1500 Oe, in such a way that a new set of variable-temperature curves were measured under this optimum field. As anticipated, the curves showed two maxima, especially those corresponding to the high-Freq curves (4000–10000 Hz range), the main one peaking in the 4–5 K (so-called high-temperature maximum) and the weakest one around 2.5 K (low-temperature maximum, Figure 5).

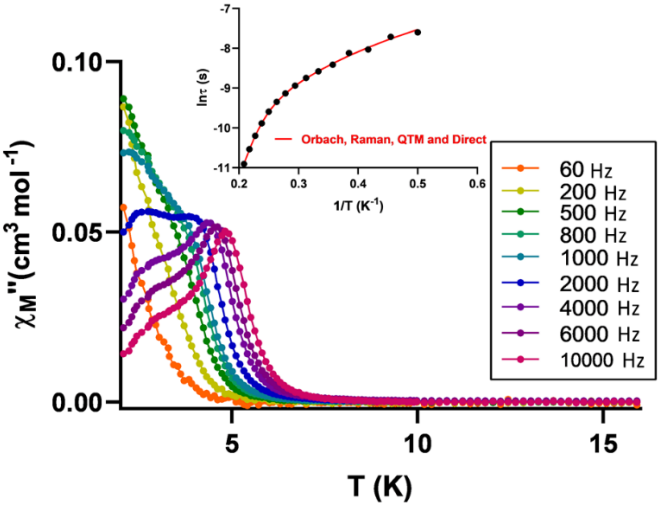

Figure 5. Temperature dependence of the χ_M'' signals for the diluted compound **2**$_{Y/Er}$ under an applied *dc* field of 1500 Oe. Inset shows the temperature dependence for the relaxation times and best fits of the data using eq. 2.

However, the high-temperature maximum seems to disappear for the low-Freq curves (below 1000 Hz) whereas the low-temperature maximum subtly increases, making the high-temperature maximum to remain as a shoulder for that Freq regime. Among all the curves, that recorded at 2000 Hz represents the midpoint where both maxima coexist with similar intensity. In spite of this fact, Cole-Cole plots showed semicircular shaped curves in the whole studied temperature range (Figure S15), which could be well fitted to the generalized Debye function (considering a single relaxation mechanism), meaning that the low temperature contribution has less effect in the relaxation. The α values arising from the fitting range between 0.25 and 0.04, finding a progressive decrease as the temperature increases, as expected. The analysis of the χ_M'' vs Freq plots (see Figure S16) revealed that a unique maximum is progressively shifted towards higher Freq as the temperature is increased, which represents the typical behaviour for SMMs. Therefore, assuming that the slow magnetic relaxation of this compound could result from the sum of two independent processes, a fact supported by the temperature-dependence of the high-temperature and low-temperature maxima, the τ distribution was fitted with two independent Orbach processes as a first attempt. As observed in Figure S18 (see ESI), the temperature-dependent τ distribution in the form of ln(τ) vs 1/T plot may be separated into two regimes (low-temperature maximum: 2.0–3.6 K and high-temperature maximum: 3.8–4.8 K) which fit reasonably well to the Arrhenius law (eq. 1), giving U_{eff} = 7.0 K (4.9 cm^{-1}); $\tau_0 = 1.75 \cdot 10^{-5}$ s and U_{eff} = 28.3 K (19.7 cm^{-}

^{1}); τ_0 = 5.58·10^{-8} s for the low-temperature and high-temperature maxima, respectively (see Table 3).

Nonetheless, we also turned to the possibility of considering the occurrence of multiple relaxation mechanisms operating simultaneously in the dynamics of this compound, mainly because i) the curvilinear shape of the ln(τ) vs 1/T plot and ii) the absence of two low-lying excited states from which two distinct Orbach mechanisms (or TA-QTM, Thermally Activated QTM) could occur as concluded in the computational part (vide infra). Among all the attempts made to reproduce the experimental curve by combining the Orbach, Raman, Direct and QTM mechanisms, the best result was achieved by using all of them as gathers in equation 2:

$$\tau^{-1} = \tau_0^{-1} \exp(-U_{eff}/\kappa_B T) + \tau_{QTM}^{-1} + A_{direct} T + B_{Raman} T^n \quad \text{(eq. 2)}$$

Being conscious about the risks of overparametrization related with the use of this equation, some parameters were first estimated from fitting of the isothermal field-dependence of the relaxation times as previously suggested in the bibliography, using equation 3:[16]

$$\tau^{-1} = AH^4T + B/(1 + CH^2) + D \quad \text{(eq. 3)}$$

where the three terms correspond to the direct, QTM and field-independent processes, respectively. This could be done because of the U-shape of the $\tau^{-1}(H)$ curve, which is indicative of the presence of both QTM and direct processes. At low applied fields, QTM is being quenched and consequently relaxation times are enhanced. After the maximum at 1500 Oe, the direct process becomes dominant and relaxation times are shortened in agreement with the H^4 dependence. The best fitting results gave: A = 175596 s^{-1} K^{-1} T^{-4}, B = 2055 s^{-1}, C = 325.3 T^{-2} and D = 6041 s^{-1} (see Figure S17), values that were introduced as constraints (for QTM and direct processes) in equation 2 to obtain a reasonable fitting: τ_0 = 1.47·10^{-10} s and U_{eff} = 58.5 K (40.6 cm^{-1}, for Orbach), τ_{QTM} = 4.05 10^{-3} s, A_{direct} = 88.9 s^{-1} K^{-1}, B_{Raman} = 187 s^{-1} K$^{-2.9}$ and n = 2.9 (see inset in Figure 5). Moreover, the presence of double-phonon relaxation involving the Raman process, as well as the anomalous low Raman exponent could be the result of the experimental conditions: a strong magnetic field (1500 Oe) and low temperature (close to 2 K), both of which may trigger this process according to the study conducted by Gu and Wu.[63] These values, found within the range reported for other published Er-based SIMs,[64] could be considered reliable because they are supported by the *ab initio* calculations performed (vide infra).

***Ab initio* calculations**

With the aim of understanding the single-ion relaxation processes taking place in these compounds, complete active space self-consistent field (CASSCF) calculations were performed. To assess the effects arising from the coulombic and structural features of the model on the properties, several models of $\mathbf{1_{Dy}}$ were evaluated, involving the optimization of the hydrogen atoms and the inclusion of neighbouring sodium coordination environments. A detailed analysis of the results of these models reveals a clear dependency of the energy and composition of the lowest lying Kramers doublets (KDs) on the inclusion of sodium counterions (see all results inS8 section of the ESI). In particular, the directions of the easy axes of the ground and first excited states seem to switch among them for the different models. Such a dependency on the model is not fully unexpected and has been deeply discussed for the compound of [Na{Dy(DOTA)(H$_2$O)}]·4H$_2$O formula, where a large sensitivity of the energy of the first excited state as a function of the Madelung potential, arising from the presence of low-energy excited states with an almost perpendicular direction of the easy axis.[65,66] Taking into account that both effects are present in our case, a fifth model consisting of the complex including two surrounding sodium ions, that is, the [Dy(6m2onic)$_4$Na$_2$(H$_2$O)$_6$] fragment (model 5-Dy, hereafter), on which point charges on a previous computation (see Computational details) were included in order to reproduce the Madelung potential and provide a more accurate description of the experiments. As observed, this model reproduced well the experimental $\chi_M T$ vs T and M vs H curves, which ensured its validity (see Figure 3), so an equivalent model was used to describe the theoretical results of compound $\mathbf{2_{Er}}$. Starting with model 5-Dy, the results show a moderate crystal field that splits the eight KDs generated from the ground $^6H_{15/2}$ term by 302 cm^{-1} (Table 4) which is consistent with the ligand field usually observed for lanthanide(III) ions.[67–69] The ground KD presents sizeable easy-axis anisotropy denoted by the small transverse components and large axial component that is close to the value corresponding to a pure m_j = 15/2 (g_z = 20, note that it presents a dominant $|\pm15/2\rangle$ character yet somewhat admixed with $|\pm13/2\rangle$). The axiality slightly decreases for the excited KDs and becomes minimal for the 4th excited state, whereas it progressively increases again when moving to higher energy KDs.

Table 4. Energy spectrum and g tensors for the eight KDs arising from the ground state of compound $\mathbf{1_{Dy}}$ calculated on model 5-Dy.

Energy (cm^{-1})	g_x	g_y	g_z	Angle of g_{zz} between ground and higher KDs (°)
0.00	0.17	0.32	18.54	–
31.87	0.05	0.42	15.32	41.09
74.95	0.68	1.31	13.22	26.55
128.42	0.96	2.82	8.56	29.71
173.18	3.59	4.91	6.81	77.00
203.16	1.46	4.65	13.98	70.53
258.28	0.01	0.07	19.53	70.51
301.72	0.03	0.07	19.70	31.12

To determine the relaxation processes associated with the single-ion anisotropy of the Dy(III)-based coordination centre, the transition matrix elements between the KDs were computed (Figure 6). As observed, the probability of QTM at the ground state is rather small (0.13 μB) owing to the dominant axial character and is even smaller for the thermally-assisted QTM (TA-QTM) through the first excited state (0.096 μB), while it increases substantially for the following excited states (see Figure S29.[70] In this sense, the Orbach process involving ground and first excited states presents quite high probability (2.21 μB) and involves an energy barrier of 31.9 cm^{-1}, which fits perfectly well the experimental barrier found under zero *dc* field (30.3 cm^{-1}). The good agreement found between the calculated and

experimental barrier is a consequence of the inclusion of point charges in the model, which somehow simulates the intermolecular and hyperfine interactions occurring in the crystal structure.[71] On the other hand, the excitation of the ground to the second excited state, which is largely admixed (with a dominant |*±9/2*> character and minor contributions from |*±11/2*> and |*±7/2*>), also has a high probability (2.09 μB) although it is farther in energy (75.0 cm^{-1} above the ground state, see Figure S29). However, taking into account the relatively large angle established between the g_{zz} of the KDs of the ground and first excited states (above 10°), the ground → second excited state relaxation must be considered unlikely to occur (see also Figure S19 in the ESI).[54]

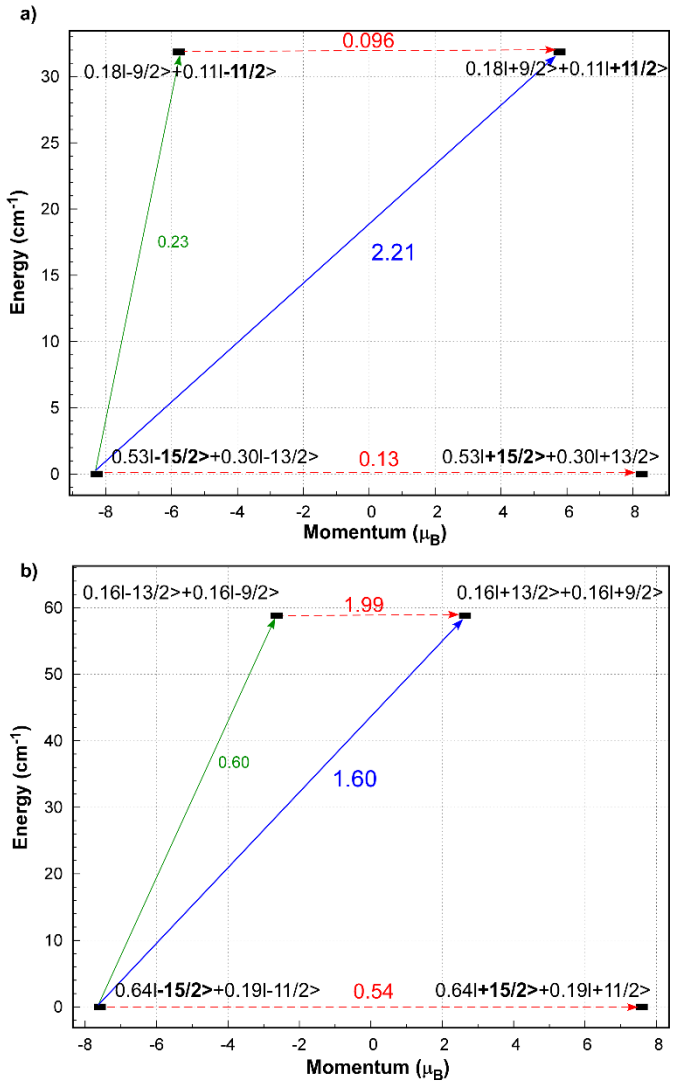

Figure 6. *Ab initio* computed relaxation mechanism on model 5-Ln showing the lowest KDs with the main wavefunctions of compounds: **(a) 1_{Dy}** and **(b) 2_{Er}**. Blue and green lines indicate the Orbach and Raman relaxation pathways for magnetization reversal mechanism through excited states. The dotted red lines represents the ground state QTM and TA-QTM via excited KDs. The numbers close to each arrow designate matrix elements of transition magnetic moment.

Concerning the compound **2_{Er}**, the results show that the low-lying KDs (the ground but especially the first excited state) are much more mixed than in the Dy-based counterpart, even though the ground state preserves a main axial character (64% in $m_J = \pm 15/2$ and $g_x = 0.68$, $g_y = 2.54$, $g_z = 15.18$). Moreover, the large matrix elements calculated for ground state QTM and TA-QTM (0.54 and 1.99 μB) are in good agreement with our aforementioned interpretation of the experimental data. On the one hand, the absence of SMM behaviour under zero applied *dc* field is clearly supported by the large value of 0.54 μB between the ground KDs. On the other hand, this same fact encouraged us to include the QTM process within the fit of the experimental data even if the application of a relatively large H_{dc} field partially suppressed it. Additionally, the large probability for the ground state → first excited state excitations (1.60 and 0.60 μB) make one think that Orbach process could be as well taking place. Although the theoretically calculated energy gap between the ground and first excited state is reasonably concordant (slightly overestimated) compared to the experimental one (58.9 vs 40.6 cm^{-1}), the greater difference (in comparison to the Dy counterpart) might be explained by the simultaneous occurrence of several other relaxation pathways (Raman, Direct and QTM) that effectively shortcut the energy gap. Note that for **$1_{Y/Dy}$** only Orbach mechanisms have been considered in order to fit the relaxation times, whereas for **$2_{Y/Er}$** additional Raman, direct and QTM processes have been suggested. In this line, it is worth noticing that, as recently discussed in the work by Sessoli, Lunghi and coworkers,[72] the occurrence of Orbach processes with low energy barriers cannot really discard the possibility that Raman processes could be as well operating. This is a consequence of the fact that Raman relaxation between two spin states (named as *a* and *b*) involves a contribution from all of the other spin states (*c*), which implies the existence of virtual states representing the contribution of this envelope of intermediate states. It must not be forgotten that these virtual states do not admit a real transition any of spin states *c* but that they only represent spin states that are no longer eigenstates of the system and thus derived from the admixture KDs caused by the phonons. Therefore, in the absence of more sophisticated calculations, such as those described the above mentioned work,[72] involving the vibrational contribution of the system, herein computed states may represent both Orbach and Raman relaxations.

As it is known, β-diketone-based local ligand-field D_{4d} and D_{2d} symmetries are desired to design good mononuclear SMMs, especially for ions possessing an oblate electron density distribution such as Dy(III) and Tb(III), because placing the electron density of the ligands above and below the *xy* plane maximizes their axial anisotropy.[26] However, as observed in the present study, SMM behaviour occurs for Dy- and Er-based counterparts whereas the Tb-based one presents no significant magnetic relaxation. With respect to the Dy- and Er-based compounds, it must be pointed out that the coordination geometry acquired by the metal centre for the present structures is somewhat distorted and, though close to a SAPR (S = 0.458, D_{4d}), it is not too far from BTPR (S = 1.824, C_{2v}) and TDD (S = 1.992, D_{2d}) as confirmed by SHAPE program. In fact, a detailed analysis of the DyO_8 coordination centre reveals that the anisotropy axis (Figure 7a), bearing in mind that it extends parallel to oblate density, is located close to the O31C and O31D carboxylate oxygen atoms because these impose the smallest Ln–O coordination distances (see Table 1). This situation does not obey the ideal placement of the axis found in the high-performance SMMs such as the sandwhich-type complexes of $\{TbPc_2\}$[73] and $[DyLz_2(o\text{-vanilin})_2]\cdot$anion$\cdot$solvent (where Lz = 6-pyridin-2-yl-[1,3,5]triazine-2,4-diamine)[74] formulae, which also explains the partial, but not ideal, axiality achieved in the ordering of the |J_Z> states (dominant |*±15/2*> ground state but

more weakly magnetized and largely admixed first excited state, (see Figure 6).

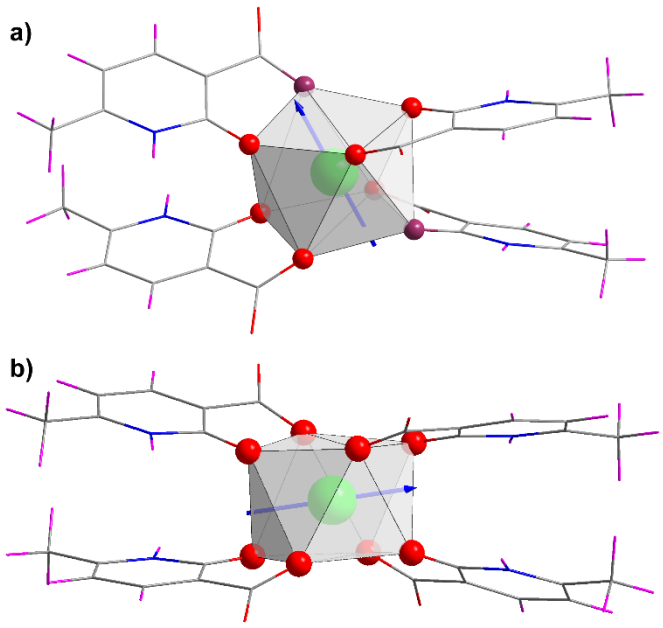

Figure 7. Views of the [Ln(6m2onic)$_4$] excerpts showing the SAPR polyhedron and computed magnetic anisotropy axes (blue arrow) for **a) 1-Dy** (where O31C and O31D atoms are coloured in dark red) and **b) 2-Er**.

Probably as a consequence of the non-ideal axiality of this environment for oblate ions, it may somehow fit the axiality of a prolate-like Er(III) ion and trigger its SMM behaviour. In fact, as shown in Figure 7b, the distorted coordination environment brings an appropriate ligand-field that locates the anisotropy axis in a horizontal arrangement, in such a way that the Stark levels acquire a partial axial order with the ground state having a main |*±15/2*> but somewhat mixed excited states (see Figure 6b). Therefore, it may be concluded that these calculations support well the coexistence of all the relaxation processes and, in turn, explain the somewhat worse SMM properties of the Er-based compound compared to the Dy-based counterpart, since the magnetization reversal of the former does not need to fully overcome an energy barrier in the relaxation.

Coming back to the $[Dy(Cp)_2]^+$ and $[Er(COT)_2]^-$ examples and as a conceptual explanation of our results, we may assume our coordination sphere as an intermediate situation for stabilizing Ising ground states of m_J = ±15/2 in both Dy(III) and Er(III) ions. In order to enhance the anisotropy of Dy(III) ions, the negatively charged donor atoms should be, as strictly as possible, within the *z* axis and, at the same time, the equatorial ligand field should be as weak as possible, as it is successfully met in $[Dy(Cp)_2]^+$ compounds. Thus, the ground states are of (almost) pure Ising type followed by well separated excited states with successive m_J values, which retains great axiality. At first glance, COT^{2-} ligands might be considered similar to Cp counterparts and, therefore, appropriate for enhancing the axiality of Dy(III). However, as previously mentioned, $[Er(COT)_2]^-$ analogues display much better SMM properties than Dy(III) based compounds, in agreement with the fact that the π-bonding molecular orbitals provide predominantly an equatorial ligand field that yields Ising type ground state for Er(III) analogues.

In our specific case, the SAPR geometry was thought to suit better to the Dy(III) ion. As proven in $\mathbf{1_{Y/Dy}}$, that goal is partially achieved since it exhibits zero field SMM behavior and a relatively pure ground state but somewhat mixed ESs which do not follow the desired order, making that relaxation through the first excited state occurs. Regarding $\mathbf{2_{Y/Er}}$, the poorer properties were somehow expected due to the mentioned geometry and, accordingly, the wavefunctions describing the ground and excited states display a remarkable mixing with a subsequent ground QTM. In any case, the energy separation between the first two KDs is comparable to the Dy(III) counterpart. Compared to the ideal environment of Cp based compounds, with electron density somehow concentrated in a strict *z* axis, the area occupied by the oxygen donor atoms in these SAPR polyhedra of herein presented compounds is more extended and is closer to a COT^{2-} cycle, being able to suit to both Dy(III) and Er(III) ions. Therefore, the difference in dynamic magnetic properties for $\mathbf{1_{Y/Dy}}$ and $\mathbf{2_{Y/Er}}$ is not so large.

Conclusions

Two isostructural heterometallic CPs based on dysprosium(III) or erbium(III), 2-oxonicotinate (6m2onic) ligand and sodium cations were synthesized and physico-chemically and structurally characterized. Within the 1D structural motifs, the lanthanides reside in distorted eight-coordinate square antiprismatic environments, well isolated from each other in the crystal structure owing to the four chelating rings formed by the carboxylate/ketone moieties of 6m2onic ligands. The Dy(III)-based compound ($\mathbf{1_{Dy}}$) is the only counterpart that presents SMM behaviour under zero *dc* field, although no further analysis can be done due to the weakness of the signal. The application of an H_{dc} field of 1000 Oe boosts the signal to reveal the occurrence of two well-separated maxima, attributed to FR and SR processes. The dual relaxation is preserved in a magnetically (Y(90%)/Dy(10%), $\mathbf{1_{Y/Dy}}$) diluted sample when an optimum H_{dc} field of 1000 Oe is employed, the relaxation is best described with two Orbach processes (SR and FR). Otherwise, the relaxation fits well the Arrhenius law under zero *dc* field for $\mathbf{1_{Y/Dy}}$ with a similar result. The diluted Er(III)-based counterpart ($\mathbf{2_{Y/Er}}$) also presents a complex relaxation scenario, in which the data are nonetheless best fitted to a multiple-process relaxation that considers QTM, Orbach, Raman and direct mechanisms.

All the experimental evidence is well supported by theoretical *ab initio* calculations. Given the strong dependency of the lowest-lying KDs energy on the model computed (due to the inclusion of counterions), the Madelung potential has been simulated by the inclusion of point charges on a representative model of both compounds. On the one hand, the calculated blocking barriers and the transition matrix elements are consistent with the proposed relaxation mechanisms. In particular, an Orbach relaxation through the first excited state is the most probable pathway for the Dy(III) compound, involving an energy barrier of 31.9 cm^{-1} that fits quite well that estimated from the fitting (30.3 cm^{-1}) under zero *dc* field. In the

case of the Er(III) compound, the higher probability for not only QTM and TA-QTM but also Orbach relaxation pathways and the larger overestimation of the blocking barrier (58.9 vs 40.6 cm^{-1} for the computed vs experimental values, respectively) support the necessity of the four mechanisms in the experimental fitting. On the other hand, the ligand field generated around the lanthanide is characterized by a partial axiality on both Dy(III)- and Er(III)-based models according to the splitting of $|J_Z>$ states (with a dominant $|\pm 15/2>$ in their ground state but a mixed and weakly magnetized excited states) as well as to the transverse *g* values obtained for the following excited states. This fact is attributed to the distortion of the polyhedra with regard to an ideal SAPR, which reduces its symmetry from D_{4d} to approach it to C_{2v} and D_{2d}. As a consequence, the distorted O_8 environment is far from the ideal disposition that maximizes the axial anisotropy of oblate ions thus being able to partially adapting to the magnetic requirements of both oblate and prolate ions.

Experimental Section

Chemicals. All chemicals were of reagent grade and were used as commercially obtained with any further purification.

Synthesis of $\{[Ln(6m2onic)_2(\mu\text{-}6m2onic)_2Na(H_2O)_3]\cdot 8H_2O\}_n$ [where Ln(III) = Dy ($\mathbf{1_{Dy}}$) and Er ($\mathbf{2_{Er}}$)]. All compounds were obtained by slowly dropping an aqueous solution of the corresponding lanthanide(III) nitrate hydrated salt (0.1 mmol, using 0.0457 g for $Dy(NO_3)\cdot 6H_2O$ and 0.0443 g for $Er(NO_3)\cdot 5H_2O$) over an aqueous-methanolic solution (4 mL, 1:1) of 6m2onic (0.4 mmol, 0.0613 g). The stirring was kept constant in the mixture for several minutes while 0.5 mL of a 1M NaOH was added dropwise to fix a pH of 6 in the mixture. No precipitate was formed in this stage (Scheme 1). Finally, all solutions were allowed to evaporate at room temperature until good single crystals of $\mathbf{1_{Dy}}$ and polycrystalline powder of $\mathbf{2_{Er}}$ were obtained after 3 days. The products were collected by filtration and washed with MeOH. Yield (based on metal): 50%. Anal. Calcd for $C_{28}H_{46}DyN_4NaO_{23}$ (%): C, 33.90; H, 4.67; N, 5.65. Found: C, 34.15; H, 4.45; N, 5.83. Anal. Calcd for $C_{28}H_{46}ErN_4NaO_{23}$ (%): C, 33.73; H, 4.65; N, 5.62. Found: C, 33.63; H, 4.74; N, 5.53.

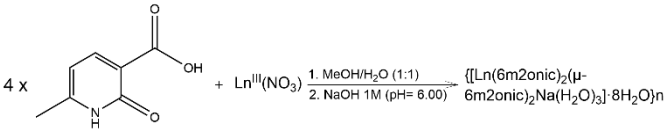

Scheme 1. Schematic drawing of the synthesis of compounds.

Chemical characterization. Elemental analyses (C, H, N) were performed on a Leco CHNS-932 microanalyzer. IR spectra were acquired on diluted KBr pellets in a ThermoNicolet IR 200 spectrometer in the 4000–400 cm^{-1} spectral region. Magnetic susceptibility measurements were carried out on polycrystalline samples of the compounds with a Quantum Design SQUID MPMS-7T susceptometer at an applied magnetic field of 1000 G. The susceptibility data were corrected for the diamagnetism estimated from Pascal's Tables,[75] the temperature-independent paramagnetism, and the magnetization of the sample holder. Alternating current measurements were performed on a physical property measurement System-Quantum Design model 6000 magnetometer under a 3.5 G *ac* field and frequencies ranging from 60 to 10 000 Hz. Thermal analyses (TG/DTA) were performed on a TA Instruments SDT 2960 thermal analyzer in a synthetic air atmosphere (79% N_2 / 21% O_2) with a heating rate of 5 °C·min^{-1}.

X-ray Diffraction Data Collection and Structure Determination. A suitable single crystal of compounds $\mathbf{1_{Dy}}$ was mounted on a Bruker VENTURE diffractometer equipped with area detector and graphite monochromated Mo K_α radiation (λ = 0.71073 Å). Data collection was performed at 130(2) K through the ω-scan method and data reduction was performed with the APEX2[76] software, correcting the absorption of the crystal with SADABS.[77] The crystal structure was solved by direct methods using the SHELXT program[78] and refined by full-matrix least-squares on F^2 including all reflections with WINGX crystallographic package.[79,80] All hydrogen atoms were located in the difference Fourier map and included as fixed contributions using riding models with isotropic thermal displacement parameters 1.2 and 1.5 times those of their parent atoms for the 6m2onic ligand and water molecules, respectively. The main crystallographic details and refinement data are gathered in Table 5. Crystallographic data has been deposited with the Cambridge Crystallographic Data Center as supplementary publication with nos. CCDC 2190996. Copies of the data can be obtained free of charge on application to the Director, CCDC, 12 Union Road, Cambridge, CB2 1EZ, U.K. (Fax: +44-1223-335033; e-mail: deposit@ccdc.cam.ac.uk or http://www.ccdc.cam.ac.uk).

Table 5. Single crystal X-ray diffraction data and structure refinement details of compound $\mathbf{1_{Dy}}$.

Compound	$\mathbf{1_{Dy}}$
Empirical formula	$C_{28}H_{46}DyN_4NaO_{23}$
Formula weight	992.18
Crystal system	orthorhombic
Space group	*Pbca*
a (Å)	18.7386(8)
b (Å)	22.8598(10)
c (Å)	18.0928(7)
V (Å^3)	7750.2(6)
Reflections collected	278149
Unique data/parameters	10013 / 518
Rint	0.0349
GoF (S)[a]	1.068
R_1[b]/wR^2[c] [I>2σ(I)]	0.0184 / 0.0477
R_1[b]/wR^2[c] [all]	0.0209 / 0.0496

[a] $S = [\sum w(F_o^2 - F_c^2)^2 / (N_{obs} - N_{param})]^{1/2}$. [b] $R_1 = \sum||F_o|-|F_c|| / \sum|F_o|$; [c] $wR^2 = [\sum w(F_o^2 - F_c^2)^2 / \sum wF_o^2]^{1/2}$; $w = 1/[\sigma^2(F_o^2) + (aP)^2 + bP]$ where $P = (\max(F_o^2,0) + 2F_c^2)/3$ with a = 0.0224 and b = 6.9327.

The X-ray powder diffraction (XRPD) patterns were measured on grounded single crystals or polycrystalline samples. A Philips X'PERT powder diffractometer, equipped with Cu-Kα radiation (λ = 1.5418 Å), was used to measure the diffractograms over the 5 < 2θ < 50° range with a step size of 0.026° and an acquisition

time of 2.5 s per step at 25 °C. Indexation of the diffraction profiles was made using FULLPROF program (pattern matching analysis)[81] on the bases of the space group and cell parameters obtained from single crystal X-ray diffraction of $\mathbf{1_{Dy}}$.

Computational details. Gaussian 16 package[82] was employed for the partial optimization of the models (1-Dy, 3-Dy and 4-Dy) used in the simulation of the magnetic properties. These models consisted of excerpts taken from the X-ray coordinates of compound $\mathbf{1_{Dy}}$, and optimizations were performed at DFT level of theory, using the UB3LYP functional[83] and the "Stuttgart/Dresden" basis sets and effective core potentials were used to describe the lanthanide(III) ions,[84] and the 6-311G++(d,p) basis set for the rest of non-metal atoms.[85] In any case, the model best representing the properties (5-Dy) was computed by adding the point charges as density derived point charges obtained from a single point calculation on the unit cell of $\mathbf{1_{Dy}}$ with periodic boundary conditions. Charge distribution of the atoms comprising the unit cell of $\mathbf{1_{Dy}}$ was obtained from periodic density-functional theory calculations performed using the code CASTEP,[86] included in the Materials Studio software.[87] The PBE exchange-correlation functional was used in the calculations,[88] along with double zeta basis sets with polarization functions and on-the-fly generated (OTFG) nom conserving pseudopotentials.[89,90] On the other hand, the *ab initio* calculations were conducted with ORCA software suite (version 5.0.2),[91,92] using the B3LYP functional.[93,94] The second-order Douglas-Kroll-Hess (DKH)[95,96] scalar relativistic Hamiltonian was used to treat the scalar relativistic effects, in combination with the recontracted def2-TZVP basis sets for all atoms except for the lanthanide atoms, for which SARC2-DKH-QZVP was employed. RIJCOSX approximation with appropriate auxiliary basis sets (SARC/J)[97] were employed to speed up all calculations. Calculations with state-average complete active space self-consistent field (SA-CASSCF) method were performed incorporating the seven f-orbitals and nine and eleven electrons respectively for $\mathbf{1_{Dy}}$ and $\mathbf{2_{Er}}$. The calculations included all the possible roots stemming from their electronic configuration (21 sextets, 224 quartets and 490 doublets for $\mathbf{1_{Dy}}$; and 35 quartets and 112 doublets for $\mathbf{2_{Er}}$). After convergence of CASSCF energies, spin−orbit coupling (SOC) effects were included in a subsequent quasi-degenerate perturbation theory (QDPT) step. Spin Hamiltonian parameters were also calculated from these converged results by means of SINGLE_ANISO code as implemented in ORCA.[98,99]

Acknowledgements

This work has been funded by the Spanish Ministry of Science, Innovation and Universities (MCIU/AEI/FEDER, UE) (PGC2018-102052-A-C22, PGC2018-102052-B-C21), University of the Basque Country (GIU20/028), Gobierno Vasco/Eusko Jaurlaritza (IT1755-22), and Junta de Andalucía (FQM-394 and B-FQM-734-UGR2). OPC thanks his predoctoral fellowship to UPV/EHU. The authors thank for technical and human support provided by SGIker (UPV/EHU/ ERDF, EU).

Notes and references

1 L. Jiao, J. Y. R. Seow, W. S. Skinner, Z. U. Wang and H.-L. Jiang, *Mater. Today*, 2019, **27**, 43–68.
2 H. Li, K. Wang, Y. Sun, C. T. Lollar, J. Li and H.-C. Zhou, *Mater. Today*, 2018, **21**, 108–121.
3 R. Medishetty, J. K. Zaręba, D. Mayer, M. Samoć and R. A. Fischer, *Chem. Soc. Rev.*, 2017, **46**, 4976–5004.
4 G. Maurin, C. Serre, A. Cooper and G. Férey, *Chem. Soc. Rev.*, 2017, **46**, 3104–3107.
5 C. T. Chen and K. S. Suslick, *Coord. Chem. Rev.*, 1993, **128**, 293–322.
6 W. Lu, Z. Wei, Z. Y. Gu, T. F. Liu, J. Park, J. Park, J. Tian, M. Zhang, Q. Zhang, T. Gentle, M. Bosch and H. C. Zhou, *Chem. Soc. Rev.*, 2014, **43**, 5561–5593.
7 X. Liu, L. Zhang and J. Wang, *J. Mater.*, 2021, **7**, 440–459.
8 V. Guillerm, D. Kim, J. F. Eubank, R. Luebke, X. Liu, K. Adil, M. S. Lah and M. Eddaoudi, *Chem. Soc. Rev.*, 2014, **43**, 6141–6172.
9 M. Eddaoudi, D. F. Sava, J. F. Eubank, K. Adil and V. Guillerm, *Chem. Soc. Rev.*, 2015, **44**, 228–249.
10 A. Ahmed, S. Seth, J. Purewal, A. G. Wong-Foy, M. Veenstra, A. J. Matzger and D. J. Siegel, *Nat. Commun.*, 2019, **10**, 1568.
11 S. Geng, E. Lin, X. Li, W. Liu, T. Wang, Z. Wang, D. Sensharma, S. Darwish, Y. H. Andaloussi, T. Pham, P. Cheng, M. J. Zaworotko, Y. Chen and Z. Zhang, *J. Am. Chem. Soc.*, 2021, **143**, 8654–8660.
12 R. Aniruddha, I. Sreedhar and B. M. Reddy, *J. CO2 Util.*, 2020, **42**, 101297.
13 J. Rocha, L. D. Carlos, F. A. A. Paz and D. Ananias, *Chem. Soc. Rev.*, 2011, **40**, 926–940.
14 J. Heine and K. Müller-Buschbaum, *Chem. Soc. Rev.*, 2013, **42**, 9232–9242.
15 J. Cepeda and A. Rodríguez-Diéguez, *CrystEngComm*, 2016, **18**, 8556–8573.
16 A. Zabala-Lekuona, J. M. Seco and E. Colacio, *Coord. Chem. Rev.*, 2021, **441**, 213984.
17 G. Mínguez Espallargas and E. Coronado, *Chem. Soc. Rev.*, 2018, **47**, 533–557.
18 T. Yamada, K. Otsubo, R. Makiura and H. Kitagawa, *Chem. Soc. Rev.*, 2013, **42**, 6655–6669.
19 U. Huizi-Rayo, J. Gutierrez, J. M. Seco, V. Mujica, I. Diez-Perez, J. M. Ugalde, A. Tercjak, J. Cepeda and E. San Sebastian, *Nano Lett.*, 2020, **20**, 8476–8482.
20 P. Dechambenoit and J. R. Long, *Chem. Soc. Rev.*, 2011, **40**, 3249–3265.
21 S. S. Nadar and V. K. Rathod, *Int. J. Biol. Macromol.*, 2018, **120**, 2293–2302.
22 J. M. Frost, K. L. M. Harriman and M. Murugesu, *Chem. Sci.*, 2016, **7**, 2470–2491.
23 I. Oyarzabal, B. Fernández, J. Cepeda, S. Gómez-Ruiz, A. J. Calahorro, J. M. Seco and A. Rodríguez-Diéguez, *CrystEngComm*, 2016, **18**, 3055–3063.
24 A. A. García-Valdivia, J. M. Seco, J. Cepeda and A. Rodríguez-Diéguez, *Inorg. Chem.*, 2017, **56**, 13897–13912.
25 A. K. Mondal, A. Mondal and S. Konar, *Magnetochemistry*,

2020, **6**, 45.
26 J. D. Rinehart and J. R. Long, *Chem. Sci.*, 2011, **2**, 2078–2085.
27 S. Maheswaran, G. Chastanet, S. J. Teat, T. Mallah, R. Sessoli, W. Wernsdorfer and R. E. P. Winpenny, *Angew. Chem. Int. Ed.*, 2005, **44**, 5044–5048.
28 G. Aromí, D. Aguilà, P. Gamez, F. Luis and O. Roubeau, *Chem. Soc. Rev.*, 2012, **41**, 537–546.
29 F. S. Santana, M. Perfetti, M. Briganti, F. Sacco, G. Poneti, E. Ravera, B. Já, F. Soares and R. Sessoli, *Chem. Sci.*, 2022, **13**, 5860–5871.
30 F.-S. Guo, B. M. Day, Y.-C. Chen, M.-L. Tong, A. Mansikkamäki and R. A. Layfield, *Science (80-.).*, 2018, **362**, 1400–1403.
31 C. A. Gould, K. R. McClain, D. Reta, J. G. C. Kragskow, D. A. Marchiori, E. Lachman, E. S. Choi, J. G. Analytis, R. D. Britt, N. F. Chilton, B. G. Harvey and J. R. Long, *Science (80-.).*, 2022, **375**, 198–202.
32 X. C. Huang, M. Zhang, D. Wu, D. Shao, X. H. Zhao, W. Huang and X. Y. Wang, *Dalt. Trans.*, 2015, **44**, 20834–20838.
33 J. L. Liu, Y. C. Chen, Y. Z. Zheng, W. Q. Lin, L. Ungur, W. Wernsdorfer, L. F. Chibotaru and M. L. Tong, *Chem. Sci.*, 2013, **4**, 3310–3316.
34 J. L. Liu, Y. C. Chen and M. L. Tong, *Chem. Soc. Rev.*, 2018, **47**, 2431–2453.
35 L. Ungur and L. F. Chibotaru, *Phys. Chem. Chem. Phys.*, 2011, **13**, 20086–20090.
36 P. Evans, D. Reta, G. F. S. Whitehead, N. F. Chilton and D. P. Mills, *J. Am. Chem. Soc.*, 2019, **141**, 19935–19940.
37 B. M. Day, F. S. Guo and R. A. Layfield, *Acc. Chem. Res.*, 2018, **51**, 1880–1889.
38 P. Evans, D. Reta, C. A. P. Goodwin, F. Ortu, N. F. Chilton and D. P. Mills, *Chem. Commun.*, 2020, **56**, 5677–5680.
39 K. Randall McClain, C. A. Gould, K. Chakarawet, S. J. Teat, T. J. Groshens, J. R. Long and B. G. Harvey, *Chem. Sci.*, 2018, **9**, 8492–8503.
40 S. Bala, G. Z. Huang, Z. Y. Ruan, S. G. Wu, Y. Liu, L. F. Wang, J. L. Liu and M. L. Tong, *Chem. Commun.*, 2019, **55**, 9939–9942.
41 J. J. Le Roy, M. Jeletic, S. I. Gorelsky, I. Korobkov, L. Ungur, L. F. Chibotaru and M. Murugesu, *J. Am. Chem. Soc.*, 2013, **135**, 3502–3510.
42 A. A. García-Valdivia, S. Pérez-Yáñez, J. A. García, B. Fernández, J. Cepeda and A. Rodríguez-Diéguez, *Sci. Rep.*, 2020, **10**, 8843.
43 A. Rodriguez-Dieguez, S. Perez-Yanez, L. Ruiz-Rubio, J. M. Seco and J. Cepeda, *CrystEngComm*, 2017, **19**, 2229–2242.
44 O. Pajuelo-Corral, J. A. García, O. Castillo, A. Luque, A. Rodríguez-Diéguez and J. Cepeda, *Magnetochemistry*, 2021, **7**, 8.
45 S. Zhang, H. Ke, Q. Shi, J. Zhang, Q. Yang, Q. Wei, G. Xie, W. Wang, D. Yang and S. Chen, *Dalt. Trans.*, 2016, **45**, 5310–5320.
46 Y. Z. Tong, C. Gao, Q. L. Wang, B. W. Wang, S. Gao, P. Cheng and D. Z. Liao, *Dalt. Trans.*, 2015, **44**, 9020–9026.
47 G. J. Chen, Y. N. Guo, J. L. Tian, J. Tang, W. Gu, X. Liu, S. P. Yan, P. Cheng and D. Z. Liao, *Chem. – A Eur. J.*, 2012, **18**, 2484–2487.
48 G. J. Chen, C. Y. Gao, J. L. Tian, J. Tang, W. Gu, X. Liu, S. P. Yan, D. Z. Liao and P. Cheng, *Dalt. Trans.*, 2011, **40**, 5579–5583.
49 S. Adhikari, A. Sahana, B. Kumari, D. Ganguly, S. Das, P. P. Banerjee, G. Banerjee, A. Chattopadhyay, M. Fondo, J. S. Matalobos, P. Brandão, V. Félix and D. Das, *New J. Chem.*, 2016, **40**, 10378–10388.
50 L. Razquin-Bobillo, O. Pajuelo-Corral, B. Artetxe, A. Zabala-Lekuona, D. Choquesillo-Lazarte, A. Rodríguez-Diéguez, E. S. Sebastian and J. Cepeda, *Dalt. Trans.*, 2022, **51**, 9780–9792.
51 S. Gupta, M. V. Kirillova, M. F. C. Guedes Da Silva, A. J. L. Pombeiro and A. M. Kirillov, *Inorg. Chem.*, 2013, **52**, 8601–8611.
52 R. Bolligarla and S. K. Das, *CrystEngComm*, 2010, **12**, 3409–3412.
53 O. Castillo, E. Delgado, D. Hernández, E. Hernández, A. Martín, I. Martín and F. Zamora, *Cryst. Growth Des.*, 2016, **16**, 5466–5478.
54 I. Oyarzabal, J. Ruiz, E. Ruiz, D. Aravena, J. M. Seco and E. Colacio, *Chem. Commun.*, 2015, **51**, 12353–12356.
55 J. P. Costes, S. Titos-Padilla, I. Oyarzabal, T. Gupta, C. Duhayon, G. Rajaraman and E. Colacio, *Chem. – A Eur. J.*, 2015, **21**, 15785–15796.
56 Y.-N. Guo, G.-F. Xu, P. Gamez, L. Zhao, S.-Y. Lin, R. Deng, J. Tang and H.-J. Zhang, *J. Am. Chem. Soc.*, 2010, **132**, 8538–8539.
57 S. Zhang, H. Ke, X. Liu, Q. Wei, G. Xie and S. Chen, *Chem. Commun.*, 2015, **51**, 15188–15191.
58 M. Jeletic, P. H. Lin, J. J. Le Roy, I. Korobkov, S. I. Gorelsky and M. Murugesu, *J. Am. Chem. Soc.*, 2011, **133**, 19286–19289.
59 S. Da Jiang, B. W. Wang, H. L. Sun, Z. M. Wang and S. Gao, *J. Am. Chem. Soc.*, 2011, **133**, 4730–4733.
60 J. Ruiz, A. J. Mota, A. Rodríguez-Diéguez, S. Titos, J. M. Herrera, E. Ruiz, E. Cremades, J. P. Costes and E. Colacio, *Chem. Commun.*, 2012, **48**, 7916–7918.
61 F. Habib, O. R. Luca, V. Vieru, M. Shiddiq, I. Korobkov, S. I. Gorelsky, M. K. Takase, L. F. Chibotaru, S. Hill, R. H. Crabtree, M. Murugesu, F. Habib, I. Korobkov, S. I. Gorelsky, M. Murugesu, O. R. Luca, M. K. Takase, R. H. Crabtree, V. Vieru, L. F. Chibotaru, M. Shiddiq and S. Hill, *Angew. Chemie Int. Ed.*, 2013, **52**, 11290–11293.
62 N. F. Chilton, *CCFIT program, Chilt. Group, Manchester, U. K., 2014, http//www.nfchilton.com/software.html.*
63 L. Gu and R. Wu, *Phys. Rev. B*, 2021, **103**, 014401.
64 A. Dey, P. Kalita and V. Chandrasekhar, *ACS Omega*, 2018, **3**, 9462–9475.
65 M. Briganti, E. Lucaccini, L. Chelazzi, S. Ciattini, L. Sorace, R. Sessoli, F. Totti and M. Perfetti, *J. Am. Chem. Soc.*, 2021, **143**, 8108–8115.
66 M. Briganti, G. F. Garcia, J. Jung, R. Sessoli, B. Le Guennic and F. Totti, *Chem. Sci.*, 2019, **10**, 7233–7245.
67 Y. Gil, L. Llanos, P. Cancino, P. Fuentealba, A. Vega, E. Spodine and D. Aravena, *J. Phys. Chem. C*, 2020, **124**, 5308–

5320.
68 I. F. Díaz-Ortega, J. M. Herrera, Á. R. Carmona, J. R. Galán-Mascarós, S. Dey, H. Nojiri, G. Rajaraman and E. Colacio, *Front. Chem.*, 2018, **6**, 537.
69 K. R. Vignesh, D. I. Alexandropoulos, B. S. Dolinar and K. R. Dunbar, *Dalt. Trans.*, 2019, **48**, 2872–2876.
70 F. S. Delgado, J. Sanchiz, C. Ruiz-Pérez, F. Lloret and M. Julve, *Inorg. Chem.*, 2003, **42**, 5938–5948.
71 K. R. Vignesh, S. K. Langley, K. S. Murray and G. Rajaraman, *Inorg. Chem.*, 2017, **56**, 2518–2532.
72 M. Briganti, F. Santanni, L. Tesi, F. Totti, R. Sessoli and A. Lunghi, *J. Am. Chem. Soc.*, 2021, **143**, 13633–13645.
73 N. Ishikawa, M. Sugita, T. Ishikawa, S. Y. Koshihara and Y. Kaizu, *J. Am. Chem. Soc.*, 2003, **125**, 8694–8695.
74 J. Wu, J. Jung, P. Zhang, H. Zhang, J. Tang and B. Le Guennic, *Chem. Sci.*, 2016, **7**, 3632–3639.
75 A. EARNSHAW, ed. A. B. T.-I. to M. EARNSHAW, Academic Press, 1968, pp. ix–x.
76 B. A. I. Bruker Apex2, 2004.
77 G. M. Sheldrick, 1996, Program for Empirical Adsorption Correction.
78 G. M. Sheldrick, *Acta Crystallogr. Sect. A Found. Crystallogr.*, 2015, **71**, 3–8.
79 G. M. Sheldrick, *Acta Cryst.*, 2014, 3–8.
80 L. J. Farrugia, *J. Appl. Crystallogr.*, 2012, **45**, 849–854.
81 J. Rodríguez-Carvajal, *FULLPROF 2000, version 2.5d, Lab. Léon Brillouin (CEA-CNRS), Cent. d'Études deSaclay, Gif sur Yvette Cedex, Fr. 2003*.
82 M. J. Frisch, G. W. Trucks, H. B. Schlegel, G. E. Scuseria, M. A. Robb, J. R. Cheeseman, G. Scalmani, V. Barone, G. A. Petersson, H. Nakatsuji, X. Li, M. Caricato, A. V Marenich, J. Bloino, B. G. Janesko, R. Gomperts, B. Mennucci, H. P. Hratchian, J. V Ortiz, A. F. Izmaylov, J. L. Sonnenberg, D. Williams-Young, F. Ding, F. Lipparini, F. Egidi, J. Goings, B. Peng, A. Petrone, T. Henderson, D. Ranasinghe, V. G. Zakrzewski, J. Gao, N. Rega, G. Zheng, W. Liang, M. Hada, M. Ehara, K. Toyota, R. Fukuda, J. Hasegawa, M. Ishida, T. Nakajima, Y. Honda, O. Kitao, H. Nakai, T. Vreven, K. Throssell, J. A. Montgomery Jr., J. E. Peralta, F. Ogliaro, M. J. Bearpark, J. J. Heyd, E. N. Brothers, K. N. Kudin, V. N. Staroverov, T. A. Keith, R. Kobayashi, J. Normand, K. Raghavachari, A. P. Rendell, J. C. Burant, S. S. Iyengar, J. Tomasi, M. Cossi, J. M. Millam, M. Klene, C. Adamo, R. Cammi, J. W. Ochterski, R. L. Martin, K. Morokuma, O. Farkas, J. B. Foresman and D. J. Fox, 2016.
83 A. D. Becke, *Phys. Rev. A*, 1988, **38**, 3098–3100.
84 M. Dolg, H. Stoll and H. Preuss, *Theor. Chim. acta 1993 856*, 1993, **85**, 441–450.
85 V. A. Rassolov, J. A. Pople, M. A. Ratner and T. L. Windus, *J. Chem. Phys.*, 1998, **109**, 1223–1229.
86 Y. L. Huang, P. L. Qiu, J. P. Bai, D. Luo, W. Lu and D. Li, *Inorg. Chem.*, 2019, **58**, 7667–7671.
87 2017, R2.
88 J. P. Perdew, K. Burke and M. Ernzerhof, *Phys. Rev. Lett.*, 1996, **77**, 3865.
89 S. Grimme, J. Antony, S. Ehrlich and H. Krieg, *J. Chem. Phys.*, 2010, **132**, 154104.
90 S. Grimme, S. Ehrlich and L. Goerigk, *J. Comput. Chem.*, 2011, **32**, 1456–1465.
91 F. Neese, F. Wennmohs, U. Becker and C. Riplinger, *J. Chem. Phys.*, 2020, **152**, 224108.
92 F. Neese, *WIREs Comput. Mol. Sci.*, 2012, **2**, 73–78.
93 C. Lee, W. Yang and R. G. Parr, *Phys. Rev. B*, 1988, **37**, 785–789.
94 A. D. Becke, *J. Chem. Phys.*, 1993, **98**, 5648–5652.
95 M. Douglas and N. M. Kroll, *Ann. Phys. (N. Y).*, 1974, **82**, 89–155.
96 M. Reiher, *Wiley Interdiscip. Rev. Comput. Mol. Sci.*, 2012, **2**, 139–149.
97 J. D. Rolfes, F. Neese and D. A. Pantazis, *J. Comput. Chem.*, 2020, **41**, 1842–1849.
98 L. Ungur and L. F. Chibotaru, *Chem. – A Eur. J.*, 2017, **23**, 3708–3718.
99 L. F. Chibotaru and L. Ungur, *J. Chem. Phys.*, 2012, **137**, 64112.